arXiv:1907.11252v1 [astro-ph.HE] 25 Jul 2019

SN 2018 FIF: THE EXPLOSION OF A LARGE RED SUPERGIANT DISCOVERED IN ITS INFANCY BY THE ZWICKY TRANSIENT FACILITY

Maayane T. Soumagnac[1,2], Noam Ganot[1], Avishay Gal-yam[1], Eran O. Ofek[1], Ofer Yaron[1], Eli Waxman[1], Steve Schulze[1], Yi Yang[1], Adam Rubin[3], S. Bradley Cenko[4,5], Jesper Sollerman[6], Daniel A. Perley[7], Christoffer Fremling[8], Peter Nugent[2,9], James D. Neill[17], Emir Karamehmetoglu[6], Eric C. Bellm[10], Rachel J. Bruch[1], Rick Burruss[11], Virginia Cunningham[12], Richard Dekany[13], V. Zach Golkhou[10,14,15], Ido Irani[1], Mansi M. Kasliwal[16], Nicholas P Konidaris[17], Shrinivas R. Kulkarni[16], Thomas Kupfer[18], Russ R. Laher[19], Frank J. Masci[19], Jonathan Morag[1], Reed Riddle[3], Mickael Rigault[20], Ben Rusholme[20], Jan van Roestel[21], and Barak Zackay[22]

Draft of July 29, 2019

ABSTRACT

High cadence transient surveys are able to capture supernovae closer to their first light than before. Applying analytical models to such early emission, we can constrain the progenitor stars properties. In this paper, we present observations of SN 2018 fif (ZTF18abokyfk). The supernova was discovered close to first light and monitored by the Zwicky Transient Facility (ZTF) and the Neil Gehrels Swift Observatory. Early spectroscopic observations suggest that the progenitor of SN 2018 fif was surrounded by relatively small amounts of circumstellar material (CSM) compared to all previous cases. This particularity, coupled with the high cadence multiple-band coverage, makes it a good candidate to investigate using shock-cooling models. We employ the SOPRANOS code, an implementation of the model by Sapir & Waxman (2017). Compared with previous implementations, SOPRANOS has the advantage of including a careful account of the limited temporal validity domain of the shock-cooling model. We find that the progenitor of SN 2018 fif was a large red supergiant, with a radius of $R = 1174^{+208}_{-81} R_\odot$ and an ejected mass of $M_{ej} = 5.6^{+9.1}_{-1.0} M_\odot$. Our model also gives information on the explosion epoch, the progenitor inner structure, the shock velocity and the extinction. The large radius differs from previously modeled objects, and the difference could be either intrinsic or due to the relatively small amount of CSM around SN 2018 fif, perhaps making it a "cleaner" candidate for applying shock-cooling analytical models.

[1] Department of Particle Physics and Astrophysics, Weizmann Institute of Science, Rehovot 76100, Israel

[2] Lawrence Berkeley National Laboratory, 1 Cyclotron Road, Berkeley, CA 94720, USA

[3] European Southern Observatory, Karl-Schwarzschild-Str 2, 85748 Garching bei Mnchen, Germany

[4] Astrophysics Science Division, NASA Goddard Space Flight Center, MC 661, Greenbelt, MD 20771, USA

[5] Joint Space-Science Institute, University of Maryland, College Park, MD 20742, USA

[6] The Oskar Klein Centre, Department of Astronomy, Stockholm University, AlbaNova, 10691 Stockholm, Sweden

[7] Astrophysics Research Institute, Liverpool John Moores University, 146 Brownlow Hill, Liverpool L3 5RF, UK

[8] California Institute of Technology, 1200 East California Boulevard, MC 278-17, Pasadena, CA 91125, USA

[9] Department of Astronomy, University of California, Berkeley, CA 94720-3411, USA

[10] DIRAC Institute, Department of Astronomy, University of Washington, 3910 15th Avenue NE, Seattle, WA 98195, USA

[11] Caltech Optical Observatories Palomar Mountain CA 92060

[12] Astronomy Department, University of Maryland, College Park, MD 20742, USA

[13] Caltech Optical Observatories California Institute of Technology, Pasadena, CA 91125

[14] Moore-Sloan, WRF Innovation in Data Science, and DIRAC Fellow

[15] The eScience Institute, University of Washington, Seattle, WA 98195, USA

[16] Cahill Center for Astrophysics, California Institute of Technology, Pasadena, CA, 91125, USA

[17] Affiliation: Observatories of the Carnegie Institution for Science, 813 Santa Barbara Street, Pasadena, CA 91101, USA

[18] Kavli Institute for Theoretical Physics, University of California, Santa Barbara, CA 93106, USA

[19] IPAC, California Institute of Technology, 1200 E. California Blvd, Pasadena, CA 91125, USA

[20] Universite Clermont Auvergne, CNRS/IN2P3, Laboratoire de Physique de Clermont, F-63000 Clermont-Ferrand, France

[21] Division of Physics, Mathematics, and Astronomy, California Institute of Technology, Pasadena, CA 91125, USA

[22] Institute for Advanced Study, 1 Einstein Drive, Princeton, New Jersey 08540, USA

1. INTRODUCTION

In recent years, advances in the field of high-cadence transient surveys have made it possible to systematically discover and follow-up supernovae (SNe) within hours of their first light (e.g., Nugent et al. 2011; Gal-Yam et al. 2014; Yaron et al. 2017; Arcavi et al. 2017; Tartaglia et al. 2017). This offers new opportunities to understand the early stages of core collapse (CC) SN explosions and to identify the nature of their progenitor stars.

First, rapid spectroscopic follow-up in the hours following first light has led to the detection of "flash ionized" emission from infant SNe (Gal-Yam et al. 2014; Shivvers et al. 2015; Khazov et al. 2016; Yaron et al. 2017; Hosseinzadeh et al. 2018). These events show prominent, transient, high-ionization recombination emission lines in their spectra, a signature of circumstellar material (CSM) ionized by the SN shock-breakout flash ("flash spectroscopy"). Khazov et al. (2016) showed that $\sim 20\%$ of the SNe discovered by the Palomar Transient Factory (PTF) within 10 days of explosion are "flashers", while recent results from ZTF (Bruch et al, in preparation) suggest that the fraction of such events may be even higher for events observed earlier, and that CSM around CC SNe progenitors is common.

Second, observational access to the first hours following the explosion has offered a new opportunity to test theoretical models of early emission from CC SNe and constrain their progenitor properties. The handful of cases where direct pre-explosion observations of progenitors exist (e.g., Smartt 2015, and references therein) suggest that many Type II SNe arise from red supergiants, a population of stars with radii ranging from about $100\,\mathrm{R}_\odot$ to $1500\,\mathrm{R}_\odot$ (e.g., Levesque 2017, and references therein). In recent years, theorists have developed analytical models linking SN early multi-color light curves to progenitor properties, such as radius, mass, or inner structure. Recent papers by Morozova et al. (2016) and Rubin & Gal-Yam (2017) review and compare these models. In this paper, we use the model by Sapir & Waxman (2017) (SW17), which has two advantages. First, it accounts for bound-free absorption in the calculation of the color temperature, a feature that may have a large impact on the estimation of the progenitor radius. Second, it extends the previous results by Rabinak & Waxman (2011) to later times, making additional observations useful in this analysis.

Comparison between early observations of CC SNe and theoretical predictions were reported previously (e.g. by Gall et al. 2015; González-Gaitán et al. 2015; Rubin & Gal-Yam 2017; Hosseinzadeh et al. 2019). Rubin & Gal-Yam (2017) account for the limited temporal validity domain of these models - which some of the other analyses do not - but were limited to r-band observations. To our knowledge, SN 2013 fs (Yaron et al. 2017) is the only published object for which high cadence multiple-band observations are available and which was modeled with the SW17 model, using a methodology accounting for the limited temporal validity domain of this model. However, the spectroscopic observations of SN 2013 fs - the best observed "flasher" to date - show evidence for $\sim 10^{-3}\,M_\odot$ of confined CSM surrounding the progenitor. The presence of CSM casts doubt upon the validity of the SW17 model in this case, and perhaps could have pushed the best-fit

model radius found for this object ($R = 100 - 350 R_\odot$) towards the lower end of the RSG radius distribution. A "cleaner" supernova, with no prominent signatures of CSM around the progenitor, may be a more appropriate test case for the SW17 model.

In this paper, we present and analyse the UV and visible-light observations of SN 2018 fif (ZTF18abokyfk), a SN first detected shortly after explosion by the Zwicky Transient Facility (ZTF; e.g., Bellm et al. 2019; Graham et al. 2019) as part of the ZTF extragalactic high-cadence experiment (Gal-Yam 2019).

We present the aforementioned observations of SN 2018 fif in §2. In §3, we present our analysis of these observations, and the spectroscopic evidence making SN 2018 fif a good candidate for modeling. §4 is dedicated to the modeling of the shock-cooling phase of SN 2018 fif and the derivation of the progenitor parameters. We then summarize our main results in §5.

2. OBSERVATIONS AND DATA REDUCTION

In this section, we present the observations of SN 2018 fif by ZTF and the Neil Gehrels Swift Observatory (*Swift*).

2.1. *Discovery*

SN 2018 fif was first detected on 2018 August 21 at 8:46 UT by the ZTF wide-field camera mounted on the 1.2 m Samuel Oschin Telescope (P48) at Palomar Observatory. ZTF images were processed and calibrated by the ZTF pipeline (Masci et al. 2019). A duty astronomer reviewing the ZTF alert stream (Patterson et al. 2019) via the ZTF GROWTH Marshal (Kasliwal et al. 2019) issued an internal alert, triggering follow-up with multiple telescopes, using the methodology of (Gal-Yam et al. 2011). This event was reported by Fremling (2018) and designated SN 2018fif by the IAU Transient Server (TNS[23]). The SN is associated with the $B = 14.5$ mag galaxy UGC 85 (Falco et al. 1999), shown in Figure 1. The coordinates of the object, measured in the ZTF images are $\alpha = 00^h09^m26^s.55$, $\delta = +47^d21'14''.7$ (J2000.0). The redshift $z = 0.017189$ and the distance modulus $\mu = 34.31$ mag were obtained from the NASA/IPAC Extragalactic Database (NED) and the extinction was deduced from Schlafly & Finkbeiner (2011) and using the extinction curves of Cardelli et al. (1989). These parameters are summarized in Table 1.

Previous ZTF observations were obtained in the months prior to the SN explosion and the most recent non-detection was on 2018 August 20 at 9:37:26.40 UT, i.e. less than 24 hours before the first detection. We present a derivation of the explosion epoch in § 3.1.
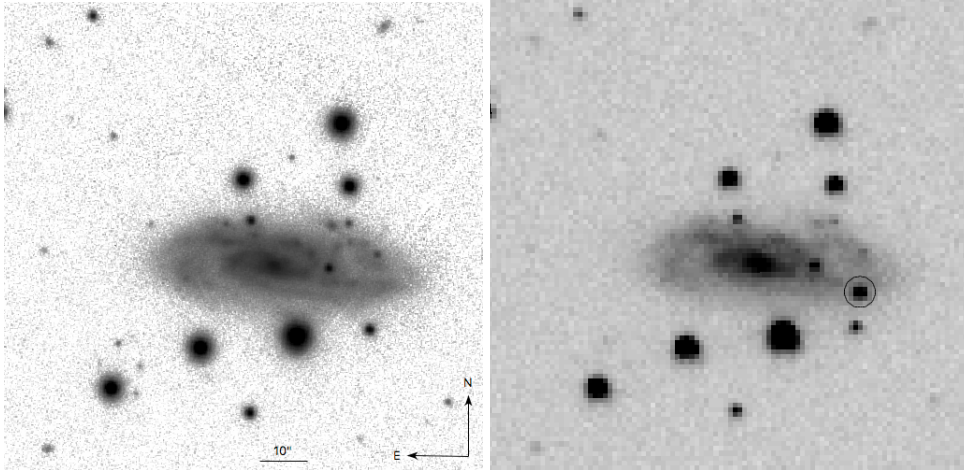
---

[23] https://wis-tns.weizmann.ac.il/

TABLE 1

Parameter	Value
Right ascension α (*J*2000)	2.360644 deg
Declination δ (*J*2000)	47.354093 deg
Redshift z	$z = 0.017189$
Distance modulus μ	34.31 mag
Galactic extinction E_{B-V}	0.10 mag

NOTE. — Basic parameters of SN 2018 fif.

FIG. 1.— Left panel: the PS1 *r*-band image[a] of UGC 85, the host galaxy of the supernova SN 2018 fif. Right panel: the P48 *r*-band image of SN 2018 fif on September 4 2018, at 9:26:50.00 UT. The circle is centered on the SN position.
[a]http://ps1images.stsci.edu

2.2. *Photometry*

SN 2018 fif was photometrically followed in multiple bands for $\sim$ 5 months. Light curves are shown in Figure 2. The photometry is reported in Table 2 and is electronically available from the Weizmann Interactive Supernova data REPository[24] (WISeREP, Yaron & Gal-Yam 2012).

Swift Gehrels et al. 2004 observations of the SN 2018 fif field started on 2018 August 21 and 11 observations were obtained with a cadence of $\sim$ 1 day.

Observations from P48 were obtained using the ZTF mosaic camera composed of 16 6K×6K CCDs (e.g. Bellm et al. 2015) through SDSS *r*-band and *g*-band filters. Data were obtained with a cadence of 3 to 6 observations per day, to a limiting magnitude of R $\approx$ 20.5 mag[AB]. ZTF data were reduced using the ZTF photometric pipeline (Masci et al. 2019) employing the optimal image subtraction algorithm of Zackay et al. (2016).

Observations from the robotic 1.52 m telescope at Palomar (P60; Cenko et al. 2006) were obtained using the rainbow camera arm of the SED Machine spectrograph (Blagorodnova et al. 2018), equipped with a 2048×2048-pixel CCD camera and g', r', and i' SDSS filters. P60 data were reduced using the FPipe pipeline (Fremling et al. 2016).

The UVOT data were retrieved from the NASA Swift Data Archive[25] and reduced using standard software distributed with HEAsoft version 6.26 [26]. Photometry was measured using the FTOOLSs uvotimsum and uvotsource with a 3 circular aperture. To remove the host contribution, we obtained and coadded two final epoch in all broad-band filters and built a host template using uvotimsum and uvotsource with the same aperture used for the transient.

2.3. *Spectroscopy*

Fifteen optical spectra of SN 2018 fif were obtained using the telescopes and spectrographs listed in Table 3.

[24] https://wiserep.weizmann.ac.il
[25] https://heasarc.gsfc.nasa.gov/cgi-bin/W3Browse/swift.pl
[26] https://heasarc.nasa.gov/lheasoft/

TABLE 2

Epoch (jd)	Mag (magAB)	Flux (10^{-17}erg/s/cm^2/Å)	Instrument
2458351.866	19.11 ± 0.06	5.756 ± 0.318	P48/R
2458351.937	18.78 ± 0.10	15.10 ± 1.391	P48/G
2458353.697	18.18 ± 0.02	15.263 ± 0.281	P60/r'
2458353.699	18.17 ± 0.03	26.563 ± 0.734	P60/g'
2458353.7021	18.23 ± 0.02	9.907 ± 0.183	P60/i'
2458352.067	18.55 ± 0.10	62.282 ± 5.992	*Swift*/UVW1
2458352.074	18.48 ± 0.23	104.091 ± 22.299	*Swift*/UVW2
2458352.132	18.71 ± 0.09	70.281 ± 6.024	*Swift*/UVM2
2458352.071	18.36 ± 0.13	40.883 ± 4.793	*Swift*/u

NOTE. — **Photometry.** This table is available in its entirety in machine-readable format in the online journal. A portion is shown here for guidance regarding its form and content.

All the observations were corrected for a galactic extinction of $E_{B-V} = 0.10$ mag, deduced from Schlafly & Finkbeiner (2011) and using Cardelli et al. (1989) extinction curves.

Following standard spectroscopic reduction, all spectra were scaled so that their synthetic photometry matches contemporaneous P48 *r*-band value. All spectra are shown in Figure 3 and are available via WISeREP.

3. ANALYSIS

3.1. *Epoch of first light*

We fitted the P48 r-band rising flux during the first week with a function of the form

$$f = a(t - t_0)^n , \qquad (1)$$

where t_0 is the time of zero flux. This allowed us to estimate the epoch at which the extrapolated r-band light curve turns to zero, which is used throughout this paper as the reference time $t_0(MJD) = 58351.1537^{+0.0356}_{-0.0903}$ (2018 Aug 21 at 03:41:19.680 UTC, 0.2 days before the first r-band detection).

3.2. *Black body temperature and radius*

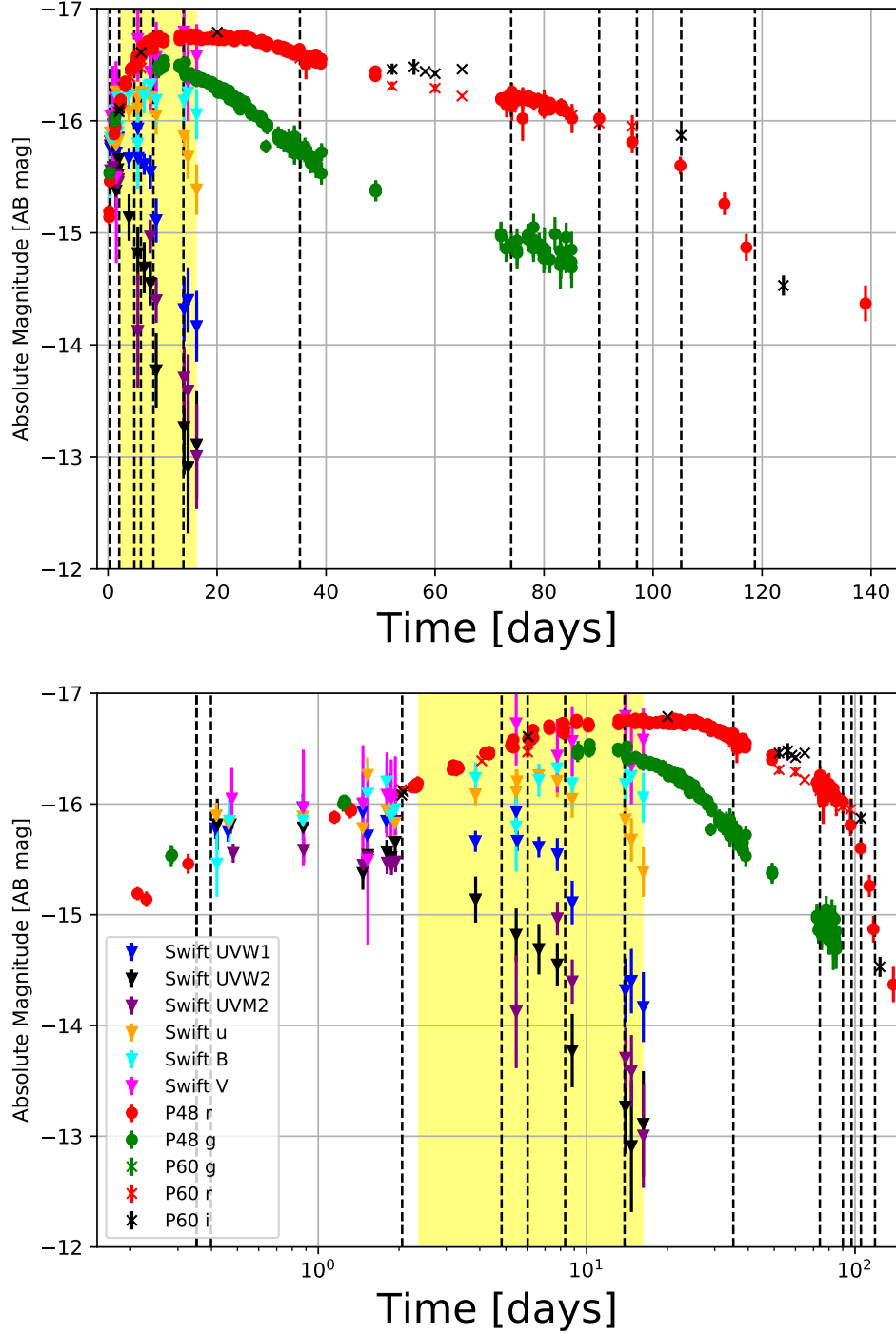Taking advantage of the multiple-band photometric coverage, we derived the temperature and radius of the

FIG. 2.— The light curve of SN 2018 fif in linear (top panel) and logarithmic space (lower panel). Time is shown relative to the estimated epoch at which the extrapolated light curve (Equation 1) turns to zero: $t_0 = 2458351.6537$, as derived in § 3.1. Black dashed lines indicate dates at which spectroscopic data exist. The yellow background indicates the validity domain of the Sapir & Waxman (2017) best fit model:$[3.735, 17.491]$ days relative to the model explosion epoch $t_{\rm ref}$, i.e. $[2.374, 16.130]$ days relative to t_0.

TABLE 3

Date (2018UT)	Phase (days)	Facility [Ref]	Exp. T (s)	Grism/Grating	Slit ('')	R	Range (Å)
08-21 12:08:32	+0.35	P200/DBSP [1]	900	600/4000+316/7500	1.5	-	3310−9190
08-21 12:08:01	+0.35	P60/SEDM [3]	2430	IFU		∼100	3700−9300
08-21 12:25:04	+0.40	Gemini N/GMOS [2]	900×4	B600	1.0	1688	3630−6870
08-23 04:59:25	+2.05	P60/SEDM [3]	1440	IFU		∼100	3700−9300
08-25 23:25:40	+4.82	LT/SPRAT [4]	300		1.8	350	4020−7960
08-27 04:22:22	+6.03	P60/SEDM [3]	1440	IFU		∼100	3780−9220
08-29 11:22:34	+8.32	P60/SEDM [3]	1440	IFU		∼100	3780−9200
09-05 03:46:42	+13.85	NOT/ALFOSC	1800	Grism 4	1.0	360	3410−9670
09-25 08:33:17	+35.20	P60/SEDM [3]	1440	IFU		∼100	3780−9220
11-03 02:50:19	+73.96	P60/SEDM [3]	1600	IFU		∼100	3780−9220
11-14 07:53:52	+85.17	P60/SEDM [3]	1200	IFU		∼100	3780−9220
11-19 06:25:58	+90.11	P60/SEDM [3]	1200	IFU		∼100	3780−9220
11-26 04:39:18	+97.04	P60/SEDM [3]	1200	IFU		∼100	3780−9220
12-04 07:48:03	+105.17	P60/SEDM [3]	1200	IFU		∼100	3780−9220
12-17 20:01:45	+118.68	WHT/ACAM [5]	1500×2	V400	1.0	450	4080−9480

NOTE. — Spectroscopic observations of SN 2018 fif. [1]:Oke & Gunn (1982); [2]:Oke et al. (1994); [3]:Blagorodnova et al. (2018); [4]:Steele et al. (2004); [5]:Benn et al. (2008)
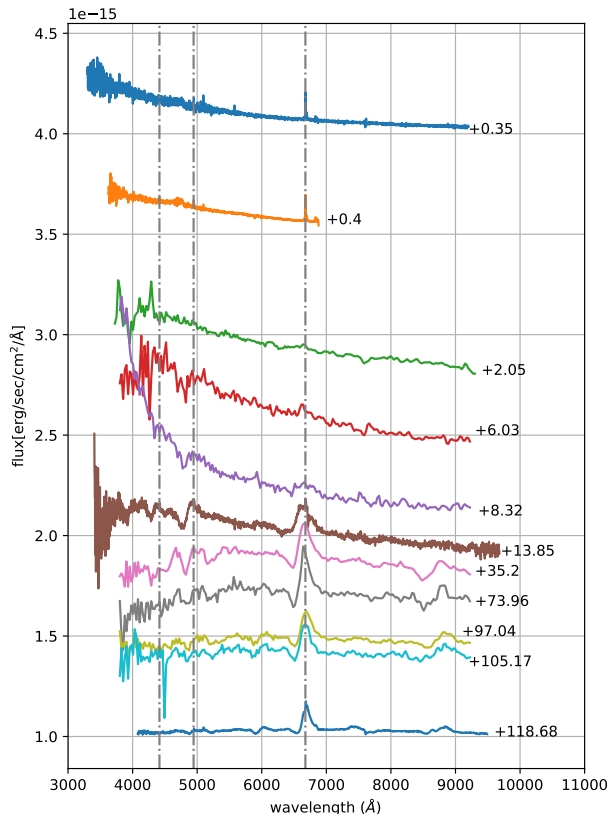
FIG. 3.— The observed spectra of SN 2018 fif. An offset was applied for easier visualization. Dashed lines indicate the redshifted emission lines for the Balmer series up to Hγ. The phase is shown relative to the estimated epoch at which the extrapolated r-band light curve (based on Equation 1) turns to zero: $t_0 = 2458351.6537$ (2018 August 21), as derived in § 3.1. A color version of this figure is available in the online journal.

black body that best fits the photometric data at each epoch after interpolating the various data sets to obtain data coverage at coinciding epochs, and deriving the errors at the interpolated points with Monte Carlo Markov-chain simulations. This was performed using the `PhotoFit`[27] tool, which is released in the appendix. The extinction E_{B-V} was implemented using the extinction curves by Cardelli et al. (1989) with $R_V = 3.08$. The interpolated SEDs are shown in Figure 4. The derived best-fit temperatures T_{BB} and radii r_{BB} are shown and compared to those derived for SN 2013 fs in Figure 5.

3.3. Bolometric light curve

Based on the measurement of r_{BB} and T_{BB}, we were able to derive the luminosity $L_{BB} = 4\pi r_{BB}^2 \sigma T_{BB}^4$ of the blackbody fits, shown in Figure 6. It is interesting to note that the bolometric peak occurs early on during the UV-dominated hot shock-cooling phase, well before the apparent peak at visible light.

3.4. Spectroscopy

Figure 3 shows the spectroscopic evolution of SN 2018fif over 119 d from its estimated explosion time.

The sequence is quite typical for Type II SNe (Gal-Yam 2017), initially showing blue, almost featureless spectra, with low-contrast Balmer lines emerging and becoming pronounced after about a week. The spectrum at phase 13.85 d is typical for the early photospheric phase, with a relatively blue continuum and strong Balmer lines, with Hα showing a strong emission component, Hβ having a symmetric P-Cygni profile, and Hγ appearing only in absorption. The spectra continue to develop during the slowly declining light curve phase over several months, with the continuum emission growing redder and lines becoming stronger. The latest spectra approach the nebular phase and are dominated by a strong emission component of the Hα line, emerging emission lines of Ca II (at $\lambda\,7300$ Å as well as the NIR triplet), weaker OI ($\lambda\,7774$ Å and a hint of $\lambda\,6300$ Å) and Na D.

Focusing on the earliest phase, in Figure 7, we show a comparison of the early spectra of SN 2018 fif (P200/DBSP and Gemini-N/GMOS at +8.4 and +8.7 hrs from the estimated explosion time, respectively) with the +21 hr NOT/ALFOSC spectrum of SN 2013 fs (Yaron et al. 2017), which is most similar to our data. We note that earlier spectra of SN 2013 fs at similar phase to those of SN 2018fif ($6-10$ h after explosion) are dominated by very strong emission lines of OIV and HeII that are not seen in this case.

In the spectrum of SN 2013 fs, the hydrogen Balmer lines show a broadened base and characteristic electron-scattering wings that are a measure of the electron density in the CSM. The spectra of SN 2018 fif do not show such electron-scattering signatures, even at a much earlier time, and the narrow emission lines seem to arise only from host galaxy emission, with similar profiles to other host lines (such as NII and SII, evident right next to the Hα line). A signature of some CSM interaction may appear in the blue part of the spectrum, in a ledge-shaped emission bump near $\lambda\,4600$ Å. This shape is similar to that seen in the SN 2013fs spectrum, though the sharp emission spikes (in particular of HeII $\lambda\,4686$ Å) are less well defined. The inset in Figure 7 shows a zoom-in of the elevated region around the HeII $\lambda\,4686$ Å, emission line for both the SN 2018 fif +8.7 hr and the SN 2013 fs +21 hr spectra. Possible emission lines that may contribute to this elevated emission region include NV $\lambda\,4604$, NII λ $4631, \lambda\,4643$ and CIV $\lambda\,4658$ Å. Although these identifications are not certain (since they are based on single lines that are only marginally above the noise level), it appears likely that a blend of high-ionization lines is responsible for the elevated emission above the blue continuum.

The difference between the spectra of SN 2013 fs and SN 2018 fif at ~ 8 hrs, and in particular the fact that SN 2013 fs showed much stronger lines of higher ionization species at similar epochs, suggests that the progenitor of SN 2018 fif was surrounded by less nearby CSM than the progenitor of SN 2013 fs. The lack of strong high-ionization lines in the spectra of SN 2018fif, as well as the sharp profiles of the Balmer lines that show no evidence of electron-scattering wings, suggest that the CSM that did surround the progenitor of SN 2018 fif was likely less dense than in the case of SN 2013 fs.

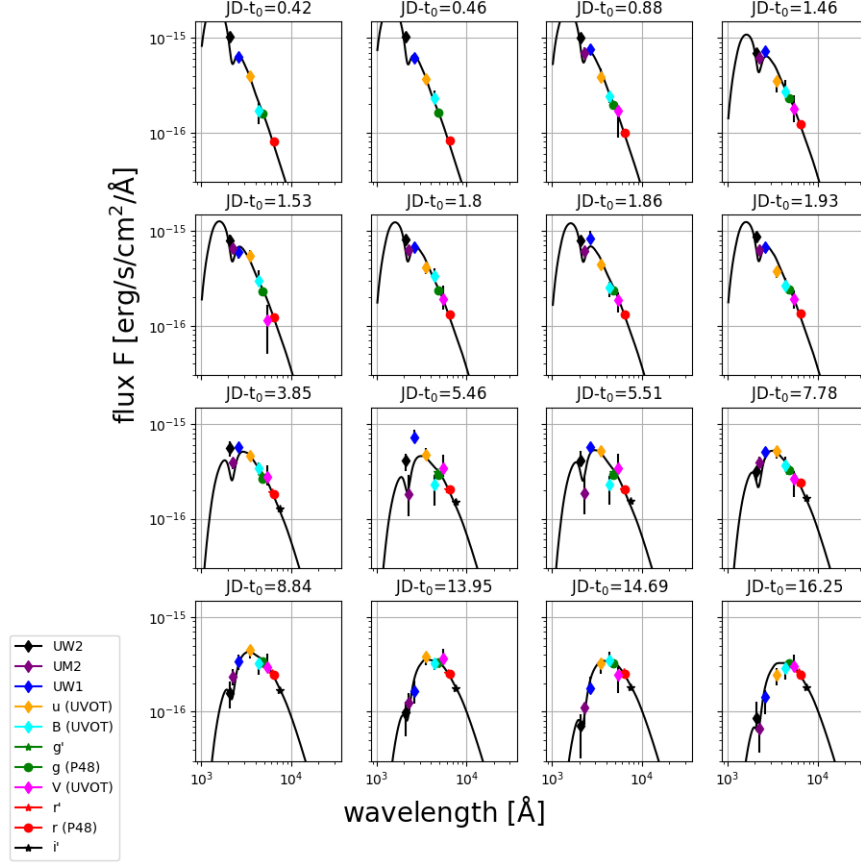## 4. SHOCK COOLING AND PROGENITOR MODEL

4.1. The model

FIG. 4.— Black body fits to Swift/UVOT and optical photometry for SN 2018 fif. Using the `PhotoFit` tool[a], photometric points were interpolated to a common epoch (UVOT epochs), and the errors at the interpolated points were computed with Monte Carlo Markov-chain simulations.

[a]https://github.com/maayane/PhotoFit

In order to model the multiple-bands emission from SN 2018 fif, we used the model by Sapir & Waxman (2017), an extension of the model derived in Rabinak & Waxman (2011). In the following, the abbreviations "SW17" and "RW11" are used to refer to the models. We summarize below the main conclusions of these two models. Both hold for temperatures > 0.7 eV, the limit above which Hydrogen is fully ionized, where recombination effects can be neglected and the approximation of constant opacity holds.

4.1.1. *The Rabinak & Waxman (2011) model*

Rabinak & Waxman (2011) explored the domain of times when the emission originates from a thin shell of mass i.e. the radius of the photosphere is close to the radius of the stellar surface. The post-breakout time-evolution of the photospheric temperature and bolometric luminosity, are given below (see also Equation (4) of Sapir & Waxman 2017), where the prefactors correspond to power-law density profiles with $n = 3/2[3]$ for convective[radiative] envelopes (see Equation (1) in Sapir

& Waxman 2017):

$$T_{\mathrm{ph,RW}} = 1.61[1.69] \left(\frac{v_{\mathrm{s*},8.5}^2 t_{\mathrm{d}}^2}{f_\rho M_0 \kappa_{0.34}} \right)^{\epsilon_1} \frac{R_{13}^{1/4}}{\kappa_{0.34}^{1/4}} t_{\mathrm{d}}^{-1/2} \, \mathrm{eV} \, , \quad (2)$$

$$L_{\mathrm{RW}} = 2.0[2.1] \times 10^{42} \left(\frac{v_{\mathrm{s*},8.5}^2 t_{\mathrm{d}}^2}{f_\rho M_0 \kappa_{0.34}} \right)^{\epsilon_2} \frac{v_{\mathrm{s*},8.5}^2 R_{13}}{\kappa_{0.34}} \, \mathrm{erg/s} \, , \tag{3}$$

where $\kappa = 0.34 \kappa_{0.34} \, \mathrm{cm}^2 \, \mathrm{g}^{-1}$, $v_{\mathrm{s*}} = 10^{8.5} v_{\mathrm{s*},8.5}$, $M = M_0 M_\odot$, $R = 10^{13} R_{13} \mathrm{cm}$, $\epsilon_1 = 0.027[0.0016]$ and $\epsilon_2 = 0.086[0.175]$. M is the mass of the ejecta, f_ρ is a numerical factor of order unity describing the inner structure of the envelope, t_{d} is the time from explosion in days, and $v_{\mathrm{s*}}$ is a measure of the shock velocity v_{sh}: in regions close to the stellar surface, at radii such as $\delta \equiv (R - r)/R \ll 1$, v_{sh} is linked to $v_{\mathrm{s*}}$ through (Gandel'Man & Frank-Kamenetskii 1956; Sakurai 1960)

$$v_{\mathrm{sh}} = v_{\mathrm{s*}} \delta^{-\beta n} \, , \tag{4}$$

with $\beta = 0.191[0.186]$, and $v_{\mathrm{s*}}$ only depends on E, M (the ejecta energy and mass) and f_ρ (Matzner & McKee
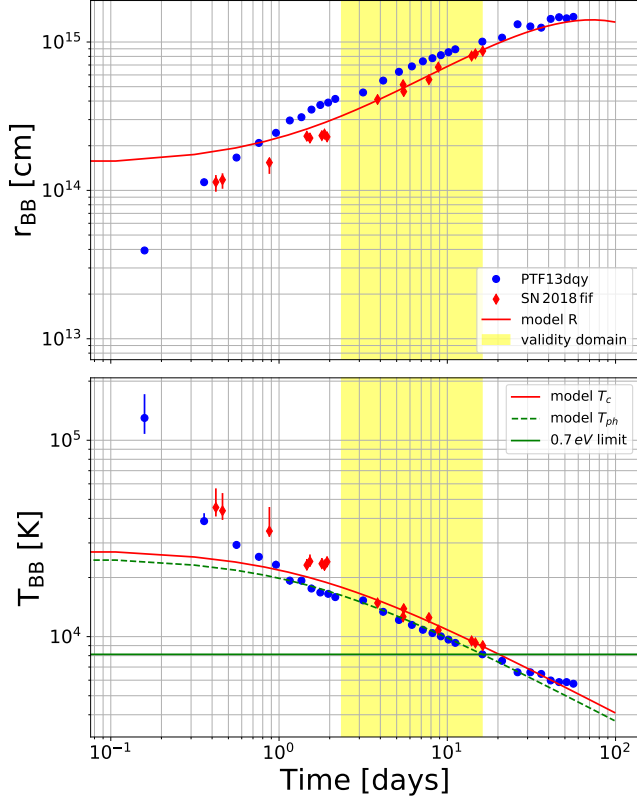
FIG. 5.— The evolution in time of: (1) the radius (top panel) and (2) the temperature (lower panel) of a blackbody with the same radiation as SN 2018 fif (red) and SN 2013 fs (blue), for comparison. For SN 2018 fif, the points were obtained by fitting a black body spectrum to the observed photometry, after interpolating the various data sets to obtain data coverage at coinciding epochs. The errors were obtained with Monte Carlo Markov-chain simulations. The SN 2013 fs results were taken from Yaron et al. (2017). The reference time for SN 2018 fif is t_0 and was obtained with a similar method for SN 2013 fs (i.e. the estimated epoch at which the extrapolated r-band light curve turns to zero). The yellow background indicates the validity domain of the Sapir & Waxman (2017) best fit model: $[2.374, 16.130]$ days relative to t_0. The red continuous line indicates the radius R and color temperature $T_{\rm col}$ predicted by SW17 for the best fit model. Note that the measured R and $T_{\rm col}$ match the prediction by SW17 on its *entire* validity range and *only* on its validity range. The green dashed line indicates $T_{\rm ph,RW}$ (linked to $T_{\rm col}$ through $T_{\rm col}/T_{\rm ph,RW} = 1.1[1.0]\pm0.05$, see section 4.1.2) and the continuous green line shows the $0.7\,eV$ temperature. The time at which $T_{\rm ph,RW}$ drops below $0.7\,eV$ defines the upper limit of the temporal validity window.

1999):

$$v_{\rm s*} \approx 1.05 f_\rho^{-\beta} \sqrt{E/M} \,, \qquad (5)$$

The RW11 model holds during a limited temporal range. The upper limit on this range,

$$t < 3 f_\rho^{-0.1} \frac{\sqrt{\kappa_{0.34} M_0}}{v_{\rm s*,8.5}} \text{ days} \qquad (6)$$

follows from the requirement that the emitting shell carry a small fraction of the ejecta mass. The lower limit

$$t > 0.2 \frac{R_{13}}{v_{\rm s*8.5}} max \left[0.5, \frac{R_{13}^{0.4}}{(f_\rho \kappa_{0.34} M_0)^{0.2} v_{\rm s*8.5}^{0.7}} \right] \qquad (7)$$
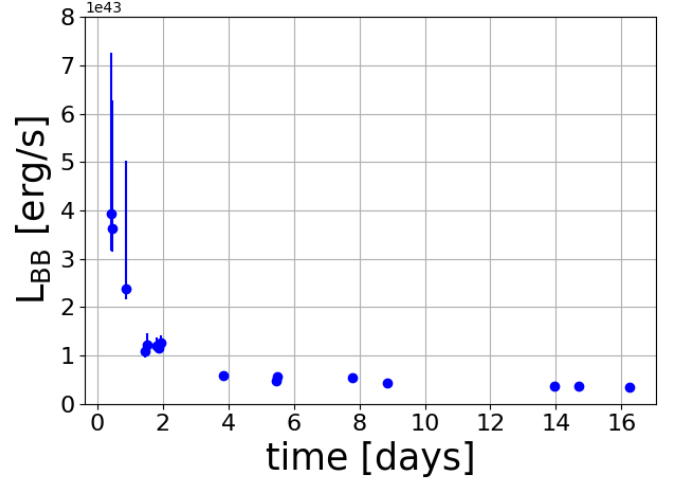

FIG. 6.— The evolution in time of the bolometric luminosity of a blackbody with the same radiation as SN 2018 fif.
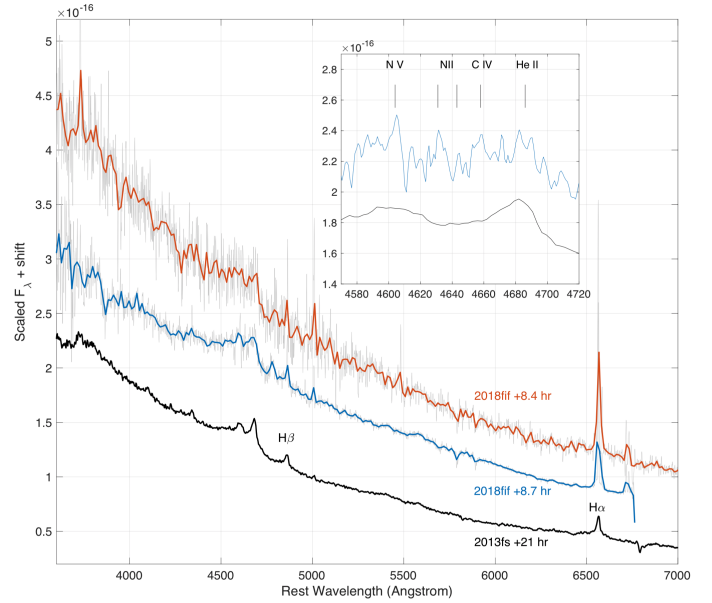

FIG. 7.— Comparison of early spectra of SN 2018 fif (at 8.4 and 8.7 hr) and SN 2013 fs (at 21 hr; from Yaron et al. 2017). SN 2018 fif shows sharp, narrow Balmer lines lacking a broad electron-scattering base. A broad ledge around 4600 Å indicates a likely blend of weak high-ionization lines, suggesting some CSM emission does exist in this event, though less than in SN 2013 fs, see text.

comes from two different requirements: (1) The photosphere must have penetrated beyond the thickness at which the initial breakout happens (see equation (16) of RW11) and (2) Expansion must be significant enough so that the ejecta are no longer planar and have become spherical (Waxman & Katz 2017); this last requirement was added to the model of Sapir & Waxman (2017).

4.1.2. The Sapir & Waxman (2017) model

Sapir & Waxman (2017) extended the RW11 description to later times, when the photosphere has penetrated more deeply into the envelope, but is still close enough to the surface so that the emission is still weakly depen-

dent on the inner structure of the envelope. As radiation originates from inner regions, the self-similar description of the shock-wave (Gandel'Man & Frank-Kamenetskii 1956; Sakurai 1960), one of the key ingredients of the RW11 model, does not hold anymore. This results in a suppression of the bolometric luminosity that can be approximated by (equation (14) of Sapir & Waxman 2017):

$$L/L_{\rm RW} = A \exp \left[- \left(\frac{at}{t_{\rm tr}} \right)^{\alpha} \right] , \qquad (8)$$

where $A = 0.94[0.79]$, $a = 1.67[4.57]$ and $\alpha = 0.8[0.73]$ for convective[radiative] envelopes. The thin shell requirement (Equation 6) is relaxed, and the new upper limit of the valid time range is dictated by the requirement of constant opacity:

$$t < min(t_{\rm tr}/a, t_{\rm T<0.7}) , \qquad (9)$$

where $t_{\rm tr}$ is the time beyond which the envelope becomes transparent, and $t_{\rm T<0.7}$ is the time when T drops below $0.7\,{\rm eV}$ and recombination leads to a decrease of the opacity.

The observed flux, for a SN at luminosity distance D and redshift z is given by

$$f_\lambda(\lambda, t) = \frac{L(t)}{4\pi D^2 \sigma T_{\rm col,z}^4} B_\lambda(\lambda, T_{\rm col,z}) \qquad (10)$$

where $T_{\rm col,z} = T_{\rm col}/(z + 1)$ is the temperature of a blackbody with intrinsic temperature $T_{\rm col}$, observed at redshift z, $T_{\rm col}/T_{\rm ph,RW} = 1.1[1.0] \pm 0.05$ for convective[radiative] envelopes, L is the bolometric luminosity given in equation 8 and B_λ is the Planck function

$$B_\lambda = \frac{2\pi hc^2}{\lambda^5} \frac{1}{e^{\frac{hc}{\lambda k_B T}} - 1} \qquad (11)$$

4.2. Interpretation of the model reference time

One of the parameters of the SW11 model is $t_{\rm ref}$. This parameter should not be confused with $t_{\rm exp}$, the real explosion time of the SN or with t_{BO}, the time at which the shock breaks out upon reaching the edge of the progenitor's surface.

$t_{\rm ref}$ is defined as follows. In the SW17 model, the photosphere radius and luminosity (the predicted observable which we fit to our data) are derived using the following relation (introduced in Rabinak & Waxman 2011) between the radius of a layer of ejected mass (with a fraction δ_m of the ejected mass) and its final velocity $v_f(\delta_m)$:

$$r(\delta_m, t) \cong v_f(\delta_m) t , \qquad (12)$$

where t is the time elapsed since $t_{\rm ref}$. This relation is based on two approximations: (1) $R_0 \delta_m$, the initial radius of the δ_m layer before the explosion, is ignored and (2) it is assumed that δ_m is already accelerated to its final velocity $v_f(\delta_m)$ (which is approximately two times the shock velocity at this layer). These two approximations are only valid after significant expansion, i.e. when $v_f t \gg R_0$, and are not valid at early times. As a result, the interpretation of $t_{\rm ref}$ as the explosion or breakout time is wrong, and the extrapolation of $t - t_{\rm ref}$ down to 0 is expected to be before the true breakout time. We

can estimate the time gap between $t_{\rm ref}$ and t_{BO} by using the approximated formula given by equation 12 and letting the radius to expand from $r = 0$ to the progenitor initial radius $r = R$. For large progenitors, e.g. with $R = 1200\,R_\odot$, we expect that $t_{BO} - t_{\rm ref} \sim 1$ day.

4.3. The SOPRANOS algorithm

The main difficulty in implementing the SW17 model is that the temporal validity domain of the model depends on the parameters of the model themselves. In other words, different combinations of the model's parameters correspond to different data to fit (Rubin & Gal-Yam 2017). One way to cope with this difficulty is to fit the data for a chosen range of times, and to retrospectively assess whether the solution is valid in this temporal window. This approach, which was taken e.g. by Valenti et al. (2014); Bose et al. (2015); Rubin et al. (2016) and Hosseinzadeh et al. (2019), is not fully satisfactory for several reasons: (1) it may limit the explored area in the parameter space, since this area is pre-defined by the choice of the data temporal window and (2) it makes it impossible to make a fair comparison between models, as the goodness of a model should be judged on nothing more or less than its specific validity range: a good model fits the data on its *entire* validity range and *only* on its validity range. It is clear that the best-fit model (and hence deduced progenitor parameters) may depend on the arbitrary choice of pre-defined data modeled, which is not a good result.

Here, we adopt a self-consistent approach and build an algorithm to find models that fit well the data included in their entire range of validity. In this sense, our approach is similar to the one adopted by Rubin & Gal-Yam (2017). The SOPRANOS algorithm (ShOck cooling modeling with saPiR & wAxman model by gANOt & SOumagnac, Ganot et al. in preparation) is available in two versions: SOPRANOS-grid, written in matlab and SOPRANOS-mcmc, written in python (Ganot et al., in preparation). The steps of SOPRANOS-grid are as follows:

- we build a 6-dimensional grid of parameters $\{R, v_{s*,8.5}, t_{\rm ref}, M, f_\rho, E_{B-V}\}$: a given point in the grid (indexed e.g. j, for clarity) corresponds to a model $\mathcal{M}_j$;

- we calculate, for each point in the grid, the time-validity domain, and deduce from it the set of N_j data points $\{x_i, y_i\}_{i\in[1,N_j]}$ (with uncertainties σ_{y_i} on the y_i values) to be taken into account in the fit of model $\mathcal{M}_j$ to the data;

- we calculate a probability for each point in the grid, using

$$P_j = PDF(\chi_j^2, \nu_j) , \qquad (13)$$

where ν_j is the number of degrees of freedom (this number varies between models, as the validity domain - and hence the number of points included in the data - varies), χ_j^2 is the chi-square statistic of the fit, for the model $\mathcal{M}_j$

$$\chi_j^2 = \sum_{i=1}^{N_j} \frac{(y_i - \mathcal{M}_j(x_i))^2}{\sigma_{y_i}^2} \qquad (14)$$

and PDF is the chi-squared probability distribution function.

The output of this procedure is a grid of probabilities, which we can compare to each other to find the most probable model. In order to have a sensitive radius measurement (the progenitor radius is measured through the explosion temperature temporal change, and the largest change occurs at early times, when the UV channels peak), we required at least three UV points to be within the time validity domain of a model. The models labeled as invalid through this procedure have non-physical parameters.

The fluxes $\mathcal{M}_j(x_i))$ are calculated based on equation 10. The extinction $E_{\mathrm{B-V}}$, a free parameter of the model, is applied to the full spectrum using the extinction curves by Cardelli et al. (1989) with $R_V = 3.08$. Synthetic photometry is then computed using the `pyphot` algorithm[28] (Fouesneau, in preparation), to convert the monochromatic fluxes f_λ into band fluxes.

The second version of the `SORANOS` algorithm, `SOPRANOS-mcmc`, uses the model probability defined in equation 13 as the input of a Markov-chain Monte Carlo simulation. No specific requirement on the amount of UV points within the time validity domain is applied.

In both cases, we apply the following flat priors for the six parameters of our model: $R \in [200, 1500]$, $v_{\mathrm{s*},8.5} \in [0.3, 1.5]$, $M \in [2, 25]$, $f_\rho \in [\sqrt{1/3}, \sqrt{10}]$ (Sapir & Waxman 2017), $t_{\mathrm{ref}} \in [2458347.5, t_0]$, $E_{\mathrm{B-V}} \in [0.1, 0.35]$. The prior on the radius R was chosen to reflect the bulk of current measurements (Davies et al. 2018; see Figure 10 and section 5 for a discussion on higher radii). The prior on $f_\rho \in [\sqrt{1/3}, \sqrt{10}]$ corresponds to the range used in the model by Sapir & Waxman (2017). The choice of priors for t_{ref}, $v_{\mathrm{s*},8.5}$ and $E_{\mathrm{B-V}} \in [0.1, 0.35]$ is the result of an iterative process (coarse to fine grid) aiming at finding the relevant location in the parameter space while limiting the memory use and running time. In all our analysis, we use $\kappa = 0.34, \mathrm{cm^2\,g^{-1}}$ and assume a convective envelope for the progenitor.

Note that our approach is similar to the one by Rubin & Gal-Yam (2017), in the sense that it is self-consistent and takes care of the time-validity issue. However, the strategy adopted to compare and discriminate between models (equation 13) is different.

4.4. Results

In Figure 9, we show the two dimensional projections of the PDF distributions obtained by fitting our model to the data, obtained with `SOPARANO-mcmc`. Computing the position of the maximum can be problematic and challenging, all the more so when the χ^2 is noisy and full of local minima. The main challenge is to choose an initial combination of parameter values to give to the minimization algorithm. Here, we calculated the PDF for all the combinations in the MCMC and used the five combinations with highest PDF as initial values to our minimization algorithm. Although we think this method is reasonable, we are aware of the difficulty of calculating the position of the maximum. This is the reason why in table 4, we show both the median values of each pa-
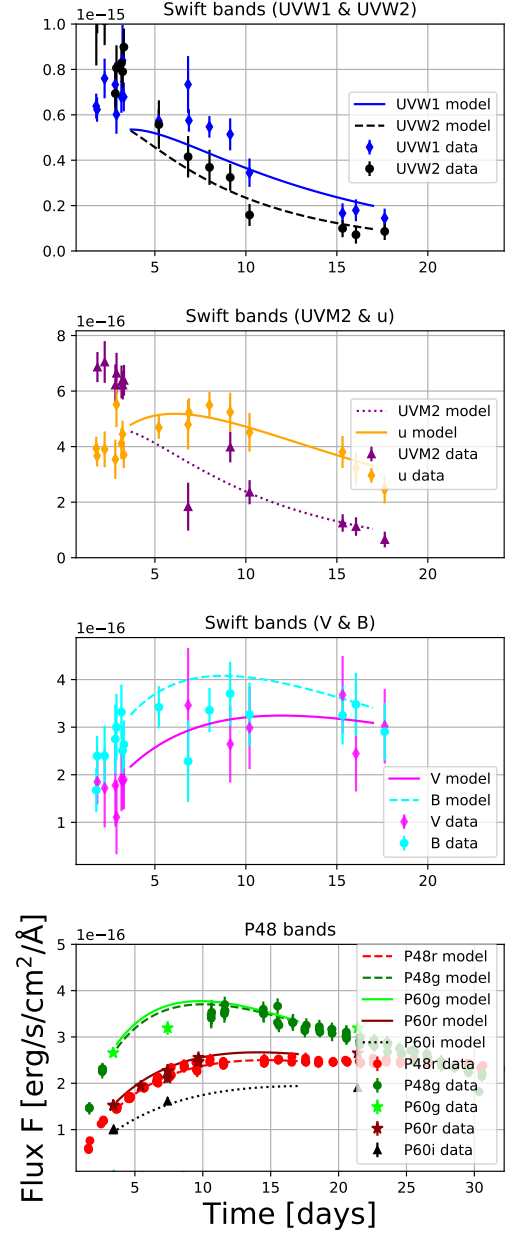
[28] http://mfouesneau.github.io/docs/pyphot/

FIG. 8.— Best fit Sapir & Waxman model ($\chi^2/dof = 0.98$) superimposed with the photometric data of SN 2018 fif. Note that here the reference date is t_{ref}, the explosion epoch predicted by our model, whereas in Figure 2, the time axis is shown relative to t_0.

rameter from its posterior distribution and the maximum likelihood point calculated by this method.

Note that when the probability function is not purely Gaussian (e.g. if it is double-peaked, which is the case here) or is asymmetric, the maximum probability does not necessarily fall close to the median of the marginalized distributions. In particular, it can fall outside of the symmetric interval containing 68% of the probability, which is often reported as the 1σ-confidence range, and does not reflect any asymmetry of the distribution. Here, we report instead the tightest intervals containing 68% of the probability and including our best-fit values.
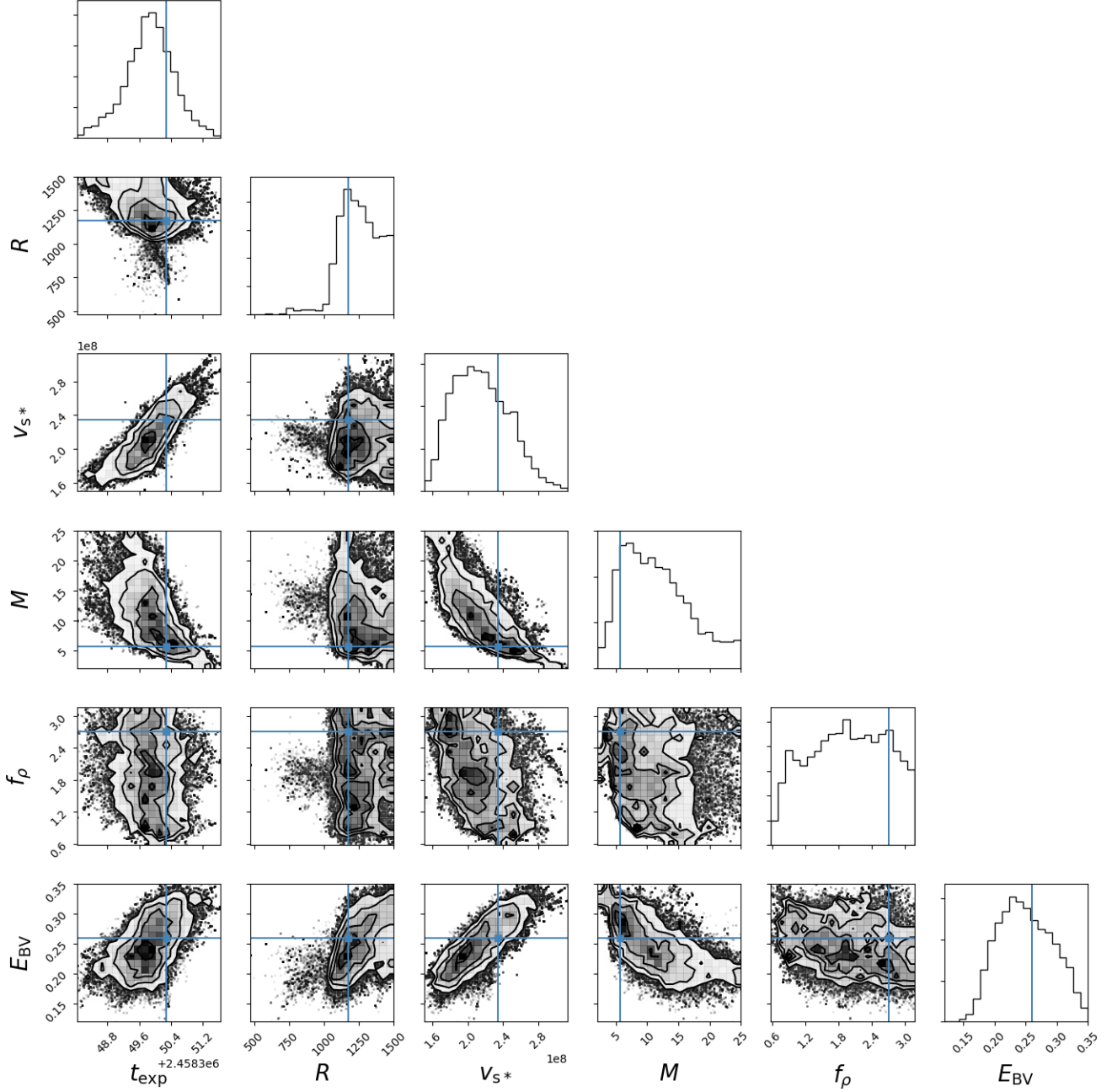
Fig. 9.— One and two dimensional projections of the posterior probability distributions of the parameters R, $v_{s*,8.5}$, M, f_ρ, t_{ref}, E_{B-V}, demonstrating the covariance between parameters. The contours correspond to the 1σ, 2σ and 3σ symmetric percentiles. The blue line corresponds to the maximum probability value calculated with the `matlab` optimizing algorithm `fminsearch`, setting the initial conditions to the maximum of the grid computed by `SOPARANO-grid`.

A full tabulation of the best-fit parameters, as well as the median and 68.2% confidence range for each parameter computed with `SOPARANO-mcmc` is shown in table 4. We checked that they are consistent with the confidence intervals computed with `SOPARANO-grid`. The best-fit parameters correspond to $\chi^2/dof = 0.98$ and are : $R = 1174^{+208}_{-81}\, R_\odot$, $M_{ej} = 5.6^{+9.1}_{-1.0}\, M_\odot$, $t_{ref} = 2458350.29^{+0.16}_{-1.01}$ JD, $E_{B-V} = 0.26^{+0.03}_{-0.07}$, $f_\rho = 2.70^{+0.22}_{-1.31}$ and $v_{s*,8.5} = 0.740^{+0.007}_{-0.198}$. The temporal validity window of this model is $[3.735, 17.491]$ days. In Figure 8, we show a comparison of the observed data and the best-fit model

and in Figure 5 we show a comparision of the blackbody temperature and radius measured from the data and predicted by the best-fit model. We comment on the best-fit results below:

- In Figure 10, we show red supergiant (RSG) radii and luminosities derived from the temperatures and luminosities measured by Davies et al. (2018) for RSGs in the small and large Magellanic Clouds (SMC and LMC). The best-fit value of the radius we find for the SN 2018 fif progenitor star, $R = 1174^{+208}_{-81}\, R_\odot$, is within but at the high end

TABLE 4

Parameter name	Best fit	Median of posterior distr.	68.2% confidence range
R	1174	1314	$[1094, 1383]$
$v_{s*,8.5}$	0.740	0.655	$[0.542, 0.747]$
M	5.6	10.6	$[4.6, 14.7]$
t_{exp}	2458350.29	2458349.67	$[2458349.29, 2458350.45]$
E_{B-V}	0.26	0.26	$[0.194, 0.286]$
f_ρ	2.7	1.87	$[1.39, 2.92]$
χ^2/dof	0.98 (107/109)	5.10 (510/100)	$-$

NOTE. — Results of the model fitting. The table shows the best-fit parameters, the median values of the MCMC chains, and 68.2% confidence range for each parameter, computed using the marginalised posterior distributions.

FIG. 10.— Radii and luminosities of the stars in the small and large Magellanic Clouds. They were derived from the effective temperatures and luminosities published by Davies et al. (2018).

of the range of radii measured for RSGs. Note that if we broaden the prior on the progenitor radius above $R = 1500\,R_\odot$, the posterior distribution becomes double peaked, exhibiting a class of solutions with large radii ($R = 2000\,R_\odot$ and above). The physical merit of such models may be questionable (Davies et al. 2018). In any case, the temporal validity window of models with such extreme progenitors starts at $t \approx t_{ref} + 15$ d, i.e. these models fit only the late-time data points, during the period the SN no longer cools at all (Fig. 5). Data sets such as ours, combined with the SW17 model, technically cannot rule out such large progenitors, if they exist.

- The value of t_{ref}, the reference time of our model, is earlier than $t_0 = 2458351.6537^{+0.0356}_{-0.0903}$ JD, the estimated epoch at which the extrapolated r-band light curve turns to zero. This is not surprising: in section 4.2 we showed that for large progenitors, e.g. with $R = 1200\,R_\odot$, the epoch of firstlight, t_{BO}, is expected to occur ~ 1 day after t_{ref}. Note also that t_0 is a measurement of the epoch of first-light in the *r-band* and hot young SNe are predicted to emit light in the UV before they significantly emit optical light: there is no reason for t_0 and t_{BO} to be strictly identical.

- The relatively high range of values of f_ρ corresponds to a high ratio of M_{env}/M_c, where M_{env} is the mass of the envelope (see Figure 5 of Sapir & Waxman 2017).

- The best-fit value of the extinction $E_{B-V} = 0.231^{+0.066}_{-0.016}\,mag$ is high: note that it is the sum of the galactic extinction $E_{B-V} = 0.10$ (deduced from Schlafly & Finkbeiner 2011 and using Cardelli et al. 1989 extinction curves) and all other sources of extinction along the line of sight, including the extinction from the SN host galaxy. The galactic extinction has a relatively high contribution to the derived value of E_{B-V}. Moreover, we used the effective wavelength of the NaD lines (in the Gemini Spectrum from August 21) in order to estimate the extinction from the host galaxy, following the relation by Poznanski et al. (2012). We found that an estimate of the host extinction is $E_{B-V,host} = 0.10 \pm 0.04$ which, summed with the galactic extinction, is consistent with the value of E_{B-V} we derived.

- In order to verify whether our best-fit value for $v_{s*,8.5}$ is consistent with the observations, we make an order of magnitude estimate of v_{sh} using equations 4 and 5 and equation 11c from Rabinak & Waxman (2011), which provides an expression of the depth δ as a function of our model parameters and link it to $v_{s*,8.5}$ and v_{sh}. We obtain that the predicted value of the velocity of the shock wave is $v_{sh} \approx 9500$ km s^{-1}. We use the P-Cygni profile of the H line in the spectrum of SN 2018 fif at $t = +13.85$ days to estimate the observed velocity $v \approx 10\,000$ km s^{-1} and find that it is consistent with the model prediction.

5. CONCLUSIONS

We presented the UV and visible-light observations of SN 2018 fif by ZTF and *Swift*. The analysis of the early spectroscopic observations of SN 2018 fif reveals that its progenitor was surrounded by relatively small amounts of circumstellar material compared to a handful of previous cases. This particularity, as well as the high cadence multiple-bands coverage, make it a good candidate to test shock-cooling models.

We employed the SOPRANOS code, an implementation of the model by Sapir & Waxman (2017): SOPRANOS-grid (matlab) and SOPRANOS-mcmc (python) (Ganot et al. in preparation). The SOPRANOS algorithm has the advantage of including a careful account for the limited temporal validity of the shock-cooling model (in this sense, our approach is similar to the one adopted by Rubin & Gal-Yam 2017).

We find that the progenitor of SN 2018 fif was a large red supergiant, with a radius of $R/R_\odot = 1174^{+208}_{-81}$ and an ejected mass of $M/M_\odot = 5.6^{+9.1}_{-1.0}$. Our model also gives information on the explosion epoch, the progenitor inner structure, the shock velocity and the extinction. The large radius differs from previously modeled objects, and the difference could be either intrinsic (differing progenitors) or due to the relatively small amount of CSM around SN 2018 fif, perhaps making it a cleaner candidate for applying shock-cooling analytical models.

As new wide-field transient surveys such as the Zwicky Transient Facility (e.g., Bellm et al. 2019; Graham et al. 2019) are deployed, many more SNe will be observed early, and quickly followed up with early spectroscopic observations and multiple-band photometric observations.

The ULTRASAT UV satellite mission (Sagiv et al. 2014) will also collect early UV light curves of hundreds of core-collapse supernovae. The methodology proposed in this paper offers a framework to analyze these objects, in order to constrain the properties of their massive progenitors and pave the way to a comprehensive understanding of the final evolution and explosive death of massive stars.

APPENDIX

RELEASE OF THE `PHOTOFIT` CODE

The `PhotoFit` tool, used to make Figure 4, Figure 5 and Figure 6 of this paper, is made available at `https://github.com/maayane/PhotoFit`. `PhotoFit` is a package for calculating and visualizing the evolution in time of the effective radius, temperature and luminosity of a supernova - or any target assumed to behave as a blackbody - from multiple-bands photometry.

Measurements in different bands are usually taken at different epochs. The first task completed by `PhotoFit` is to interpolate the flux and the errors on common epochs defined by the user. `PhotoFit` performs this task using Monte Carlo Markov Chains (MCMC) simulations.

`PhotoFit` then fits each SED with a blackbody model after (1) correcting for the extinction: PhotoFit does this using Schlafly & Finkbeiner (2011) and Cardelli et al. (1989); (3) correcting for the redshift (3) correcting for the effect of the filters transmission curves: PhotoFit does this using the `pyphot` package[29] for synthetic photometry (Fouesneau, in preparation).

The fit itself can be done in two different ways (to be chosen by the user and defined in the params.py file):

- Monte Carlo Markov Chain simulations (with `emcee`, Foreman-Mackey et al. 2013).

- A linear fit with a grid of temperatures.

REFERENCES

Arcavi, I., Hosseinzadeh, G., Brown, P. J., et al. 2017, ApJ, 837, L2

Bellm, E. C., Kulkarni, S. R., & ZTF Collaboration. 2015, in American Astronomical Society Meeting Abstracts, Vol. 225, American Astronomical Society Meeting Abstracts #225, 328.04

Bellm, E. C., Kulkarni, S. R., Graham, M. J., et al. 2019, Publications of the Astronomical Society of the Pacific, 131, 018002

Benn, C., Dee, K., & Agócs, T. 2008, in Proc. SPIE, Vol. 7014, Ground-based and Airborne Instrumentation for Astronomy II, 70146X

Blagorodnova, N., Neill, J. D., Walters, R., et al. 2018, PASP, 130, 035003

Bose, S., Valenti, S., Misra, K., et al. 2015, MNRAS, 450, 2373

Cardelli, J. A., Clayton, G. C., & Mathis, J. S. 1989, ApJ, 345, 245

Cenko, S. B., Fox, D. B., Moon, D.-S., et al. 2006, PASP, 118, 1396

Davies, B., Crowther, P. A., & Beasor, E. R. 2018, MNRAS, 478, 3138

[29] http://mfouesneau.github.io/docs/pyphot/

Falco, E. E., Kurtz, M. J., Geller, M. J., et al. 1999, Publications of the Astronomical Society of the Pacific, 111, 438

Foreman-Mackey, D., Hogg, D. W., Lang, D., & Goodman, J. 2013, Publications of the ASP, 125, 306

Fremling, C. 2018, Transient Name Server Discovery Report, 1231

Fremling, C., Sollerman, J., Taddia, F., et al. 2016, A&A, 593, A68

Gal-Yam, A. 2017, Observational and Physical Classification of Supernovae, ed. A. W. Alsabti & P. Murdin, 195

Gal-Yam, A. 2019, in American Astronomical Society Meeting Abstracts, Vol. 233, American Astronomical Society Meeting Abstracts #233, 131.06

Gal-Yam, A., Kasliwal, M. M., Arcavi, I., et al. 2011, ApJ, 736, 159

Gal-Yam, A., Arcavi, I., Ofek, E. O., et al. 2014, Nature, 509, 471

Gall, E. E. E., Polshaw, J., Kotak, R., et al. 2015, A&A, 582, A3

Gandel'Man, G. M., & Frank-Kamenetskii, D. A. 1956, Soviet Physics Doklady, 1, 223

Gehrels, N., Chincarini, G., Giommi, P., et al. 2004, ApJ, 611, 1005

González-Gaitán, S., Tominaga, N., Molina, J., et al. 2015, MNRAS, 451, 2212

Graham, M. J., Kulkarni, S. R., Bellm, E. C., et al. 2019, arXiv e-prints, arXiv:1902.01945

Hosseinzadeh, G., McCully, C., Zabludoff, A. I., et al. 2019, ApJ, 871, L9

Hosseinzadeh, G., Valenti, S., McCully, C., et al. 2018, ApJ, 861, 63

Kasliwal, M. M., Cannella, C., Bagdasaryan, A., et al. 2019, PASP, 131, 038003

Khazov, D., Yaron, O., Gal-Yam, A., et al. 2016, ApJ, 818, 3

Levesque, E. M. 2017, Astrophysics of Red Supergiants, doi:10.1088/978-0-7503-1329-2

Masci, F. J., Laher, R. R., Rusholme, B., et al. 2019, PASP, 131, 018003

Matzner, C. D., & McKee, C. F. 1999, ApJ, 510, 379

Morozova, V., Piro, A. L., Renzo, M., & Ott, C. D. 2016, ApJ, 829, 109

Nugent, P. E., Sullivan, M., Cenko, S. B., et al. 2011, Nature, 480, 344

Oke, J. B., & Gunn, J. E. 1982, PASP, 94, 586

Oke, J. B., Cohen, J. G., Carr, M., et al. 1994, in Proc. SPIE, Vol. 2198, Instrumentation in Astronomy VIII, ed. D. L. Crawford & E. R. Craine, 178–184

Patterson, M. T., Bellm, E. C., Rusholme, B., et al. 2019, PASP, 131, 018001

Poznanski, D., Prochaska, J. X., & Bloom, J. S. 2012, MNRAS, 426, 1465

Rabinak, I., & Waxman, E. 2011, ApJ, 728, 63

Rubin, A., & Gal-Yam, A. 2017, ApJ, 848, 8

Rubin, A., Gal-Yam, A., De Cia, A., et al. 2016, ApJ, 820, 33

Sagiv, I., Gal-Yam, A., Ofek, E. O., et al. 2014, AJ, 147, 79

Sakurai, A. 1960, Communications on Pure and Applied Mathematics, 13, doi:10.1002/cpa.3160130303

Sapir, N., & Waxman, E. 2017, ApJ, 838, 130

Schlafly, E. F., & Finkbeiner, D. P. 2011, ApJ, 737, 103

Shivvers, I., Groh, J. H., Mauerhan, J. C., et al. 2015, ApJ, 806, 213

Smartt, S. J. 2015, Publications of the Astronomical Society of Australia, 32, e016

Steele, I. A., Smith, R. J., Rees, P. C., et al. 2004, in Proc. SPIE, Vol. 5489, Ground-based Telescopes, ed. J. M. Oschmann, Jr., 679–692

Tartaglia, L., Fraser, M., Sand, D. J., et al. 2017, ApJ, 836, L12

Valenti, S., Sand, D., Pastorello, A., et al. 2014, MNRAS, 438, L101

Waxman, E., & Katz, B. 2017, Shock Breakout Theory, 967

Yaron, O., & Gal-Yam, A. 2012, PASP, 124, 668

Yaron, O., Perley, D. A., Gal-Yam, A., et al. 2017, Nature Physics, 13, 510

Zackay, B., Ofek, E. O., & Gal-Yam, A. 2016, ApJ, 830, 27